



# Adsorptive stripping voltammetric sensor based on Cd zeolitic imidazole framework-67 for electrochemical detection of sarin simulant

Mona Elfiky<sup>1</sup> · Amr M. Beltagi<sup>2</sup> · Osama Abuzalat<sup>3</sup>

Received: 2 August 2023 / Accepted: 21 November 2023 / Published online: 8 January 2024  
© The Author(s) 2023

## Abstract

A selective and reliable modified glassy carbon sensor, based on a 1.0% Cd zeolitic imidazole framework-67 modified glassy carbon sensor (GCS<sub>2</sub>), has been developed for ultrasensitive detection of dimethyl methyl phosphonate (DMMP) in human biological fluid. The synthesis of porous nanoparticles of Cd zeolitic imidazole framework-67 (Cd ZIF-67) was carried out via the hydrothermal method. The resulting Cd ZIF-67 powder emerges with good crystallinity, a rhombic dodecahedral morphology with particle size in the range 300~500 nm, and a specific surface area of 1780 m<sup>2</sup>·g<sup>-1</sup>. Furthermore, the fabricated sensor exhibited superior performance in the detection of DMMP with two linearity ranges of 0.02–2.0 nM and 2.0–9.0 nM and a limit of detection (LOD) of 0.06 pM. The fabricated sensor exhibited good reliability, long-term stability, and repeatability, which are favourable attributes for electroanalytical detection. In addition, the fabricated sensor displayed superior performance without significant interference during the assay of DMMP in a biological fluid (human serum sample) within two linearity ranges of 0.1–1.0 nM and 1.0–6.0 nM and a LOD of 0.03 nM.

**Keywords** Glassy carbon sensor · Modified electrode · Dimethyl methyl phosphonate · Cd zeolitic imidazole framework-67 · Stripping voltammetry · Human serum

## Introduction

Chemical warfare agents, for instance sarin, are very toxic and often fatal chemicals that pose substantial health and safety risks. Dimethyl methyl phosphonate (DMMP) (Scheme S<sub>1</sub>) has a comparable structure to sarin and is thus commonly used as a chemical warfare agent simulant [1]. Such nerve agents inhibit the acetylcholinesterase enzyme, causing the accumulation of an immoderate level of a neurotransmitter (acetylcholine) at cholinergic synapses [2].

The military threat posed by the use of these materials as chemical warfare agents increases the need for quick, efficient, and selective analytical sensors to detect such materials in different types of biological and environmental fluids [3]. DMMP has reportedly been detected using a variety of analytical techniques, including the use of several types of sensors [4–17]. In recent studies, Dipak et al. [10] and Alev et al. [13] have fabricated gas sensors based on aluminum-doped nickel ferrite nanoflakes and WS<sub>2</sub>-coated quartz crystal microbalance for the detection of DMMP in bulk form at room temperature with LODs of 0.8 μM and 0.04 μM, respectively. In addition, McKenna et al. [16] have successfully used paper spray mass spectroscopy to detect warfare agent products in the urine and blood samples with LODs of 0.1 and 0.23 μM (12.6 and 28.6 ng mL<sup>-1</sup>), respectively, as shown in Table S1. Shaik et al. have successfully fabricated *p*-hexafluoroisopropanol phenyl functionalized graphene as a strong hydrogen bond acidic polymer to interact with DMMP in its vapor state, which is considered one of the hydrogen-bond basic organophosphorus compounds using a quartz crystal microbalance (QCM) sensor [14]. As illustrated in Table S1, most of the reported methods need a

✉ Mona Elfiky  
Elfiky\_mona@science.tanta.eu.eg

✉ Osama Abuzalat  
Osama.abuzalat@mtc.edu.eg

<sup>1</sup> Department of Chemistry, Faculty of Science, Tanta University, Tanta, Egypt

<sup>2</sup> Department of Chemistry, Faculty of Science, Kafrelsheikh University, Kafrelsheikh 33516, Egypt

<sup>3</sup> Department of Chemical Engineering, Military Technical College, Cairo, Egypt

thermal analysis step to convert DMMP to its gaseous state before the main analysis process. The cyclic voltammetry technique, which uses a modified gold sensor based on the electro-polymerization of pyrrole, has only been applied by Sharma et al. [11] (Table S1) for the determination of DMMP. Due to its high selectivity and sensitivity (up to picomolar concentration levels), the adsorptive stripping voltammetry technique (AdSV) has devoted great attention to the field of sensing different species in different fluids [18]. To date, there are no detailed reports on the usage of the adsorptive stripping voltammetry technique (AdSV) for the detection of DMMP in bulk and/or biological fluids using modified electrochemical sensors. Metal–organic frameworks (MOFs) [19] are promising new adsorbent frameworks with robust adsorption and well-ordered porosity features [20]. However, the poor conductivity and stability of most MOFs reduce their usability in the field of electrochemical sensing applications. A zeolitic imidazole framework (ZIF) is a special subclass of MOFs [21], which are formed through a self-assembly method via the linking of metal ions including  $Zn^{2+}$  or  $Co^{2+}$  with organic ligands, including imidazole or imidazole derivatives. ZIFs have great potential in different applications due to their superior features such as thermal/hydrothermal stability of the framework, high specific surface area with well-ordered porosity, and robust adsorption properties [22]. ZIF-67 is a rhombic dodecahedron ZIF with a 3D pore structure [22]. Due to the redox property of  $Co^{2+}$ , which is accompanied by excellent porosity, and stability properties, ZIF-67 is a superior modifier in sensing applications [22, 23]. To improve the weakness of the conductivity property of ZIF-67 MOFs, preparation of multi-metal ZIF-67 is essential to merge the advantages of each metal ZIF material, which may improve the electrochemical sensing performance [24, 25].

In this work, porous nanoparticles of Cd zeolitic imidazole framework-67 (Cd ZIF-67) were synthesized via the hydrothermal method. Afterward, a selective and reliable modified glassy carbon sensor has been developed, based on 1.0% Cd ZIF-67 (GCS<sub>2</sub>), for ultrasensitive determination of DMMP. In addition, the as-prepared sensor was utilized to estimate DMMP in human serum samples without significant interference from the common biological interferents during the analysis process.

## Experimental part

### **Materials, apparatus, electroanalytical solutions, and the point of zero charges (pH<sub>ZPC</sub>) measurements**

This part is detailed in the supplementary material section.

## Synthesis of Cd ZIF-67 powder

In a typical synthesis, 0.34 g (1 mM) of cadmium nitrate hexahydrate and 0.291 g (1 mM) of cobalt nitrate hexahydrate were dissolved in 20 mL of methanol under stirring to prepare the metal solution. Two grams of triethylamine and 1.64 g of 2-methylimidazole were dissolved in 20 mL of methanol to prepare the ligand solution. The metal solution was then poured into the ligand solution under stirring and continually stirred for 1 h. The mixed solution was then transferred into a teflon-lined autoclave. The autoclave was placed in the oven at 60 °C for 48 h. After the reaction was done, the powder was collected, washed with methanol, and dried under vacuum at room temperature.

## Fabrication of bare and modified sensors

The bare GCSs were cleaned by polishing with a 0.05 μm alumina slurry and sonicated several times with a solution of DDW and ethanol (1:1) for 10 min. The modified GCS (GCS<sub>1</sub>) was carried out as follows: 4.0 mg of Cd ZIF-67 powder was dispersed in 1.0 mL of ethanol and 0.1 mL of a 0.5% nafion solution, followed by ultrasonication for 15 min. Then, 8.0 μL of suspension was dropped on the surface of GCS and allowed to air dry at room temperature. The same procedure was performed utilizing 8.0 mg (1.0%) and 12.0 mg (2.0%) of Cd ZIF-67 powder to fabricate GCS<sub>2</sub> and GCS<sub>3</sub>.

## Results and discussion

### The charge delocalization of DMMP

The fabrication of super-sensitive and selective electrochemical sensors mainly depends on providing diverse properties, including a low degree of resistivity ( $R_{ct}$ ), better surface area, and adsorption, as well as a better electrostatic attraction force between the proposed sensor and the solvated analyte throughout the analysis process. Therefore, the charge delocalization of DMMP was tested and estimated to be  $-1.8858431$  concerning the density functional theory (DFT) method, as illustrated in Table 1.

### Characterization of Cd ZIF-67 powder

Visual examination reveals that the reaction of cobalt and cadmium nitrate hexahydrate with 2-methylimidazole in methanol yields the pure dark brown crystalline product of Cd ZIF-67. Scanning electron microscopy confirms a rhombic dodecahedral morphology of Cd ZIF-67 and its particle

**Table 1** Data of Mulliken atomic charge of DMMP structure

Atom	Mulliken atomic charges	DMMP charge without H atoms	Overall DMMP charge
P	0.7111409	- 1.8858431	0.0
O	-0.508380		
O	-0.291168		
O	-0.443817		
C	-0.786972		
H	0.270428		
H	0.197125		
H	0.206583		
H	0.283538		
C	-0.270596		
H	0.144688		
H	0.133786		
H	0.139845		
C	-0.296051		
H	0.170421		
H	0.170230		
H	0.168931		

size distribution in the range of 300~500 nm, as shown in Fig. 1A and Fig. S1. Furthermore, the SEM-EDX demonstrated the elemental mapping distribution of Cd, C, N, and Co elements in the Cd ZIF-67 sample, proving the incorporation and uniform distribution of Cd and Co elements in the sample, as displayed in Fig. 1B.

X-ray diffraction patterns in Fig. 2A demonstrate that a pure ZIF-67 topology phase is formed, which showed similar patterns and was in good agreement with the simulated pattern [26, 27]. The comparative intensities and notable peak positions at  $2\theta = 7.3^\circ$ ,  $10.35^\circ$ ,  $12.7^\circ$ ,  $14.8^\circ$ ,  $16.4^\circ$ , and  $18^\circ$  correspond to (110), (200), (211), (220), (310), and (222), respectively. This is in good agreement with previous reports [28, 29]. The values of grain size were determined by Scherrer's equation [30].

The estimated crystallite size was 83.52 nm. As well, the FT-IR spectra in Fig. 2B further demonstrate the structural analysis of Cd ZIF-67. At higher frequencies, Cd ZIF-67 showed three contributions. The first one is a broad peak between 3500 and 3200  $\text{cm}^{-1}$  due to the stretching of the N-H bond of protonated imidazole [31, 32], and the other two are the small peaks present at 3134 and 2925  $\text{cm}^{-1}$ , which can be ascribed to C-H stretching vibrational modes of the imidazole ring and the methyl group existing in the organic ligand [33]. The peak at 1591  $\text{cm}^{-1}$  may be due to the C=N stretch modes, while the peak at 1457  $\text{cm}^{-1}$  agrees with the entire ring stretching [32]. Several spectral bands were found in the range of 1350 to 900  $\text{cm}^{-1}$  that might be related to the ring's in-plane bending. The peaks at 760 and 690  $\text{cm}^{-1}$  correspond to aromatic sp<sup>2</sup> C-H bending [34]. The peak at 425  $\text{cm}^{-1}$  corresponds to the Co-N bond [35].

Furthermore, Fig. 2C presents the N<sub>2</sub>-adsorption isotherms Cd ZIF-67, and accordingly, the BET surface area is 1780  $\text{m}^2/\text{g}$ . The obvious high surface area could confirm the effective fabrication of highly porous Cd ZIF-67.

In addition, the point of zero charges ( $pH_{pzc}$ ) is described as a pH at which the surface charge density of the surface of fabricated molecules is equal to zero [18]. In this work, the  $pH_{pzc}$  of Cd ZIF-67 was found to be equal to  $pH$  7.3, as illustrated in Fig. S<sub>2</sub>. Subsequently, at  $pH \leq 7.0$ , the net surface charge of Cd ZIF-67 is positively charged (+ve), whereas at  $pH \geq 8.0$ , the net surface charge is negatively charged (-ve).

As shown in Fig. 2D, ZIF-67 and Cd ZIF-67 were further studied using Raman spectroscopy. The peaks at 413, 468, 515, and 680  $\text{cm}^{-1}$  are attributed to ZIF-67, including the Co-N bond at 413  $\text{cm}^{-1}$  and the vibrational mode of the 2-methyl imidazolite ligand at 680  $\text{cm}^{-1}$  [36]. The peaks at 468, 515, 607, and 687  $\text{cm}^{-1}$  belonged to the four Raman active modes of  $E_g$ ,  $F^1_{2g}$ ,  $F^2_{2g}$ , and  $A^1_g$  for the Co-O bond [37]. Cd ZIF-67 spectrum (Fig. 2D) showed new peaks around 300, 510, and 590  $\text{cm}^{-1}$ . The peak around 300  $\text{cm}^{-1}$  is the 1LO (longitudinal optical) phonon arising from the A1 mode of the Cd-N bond vibration, and the peak at 590  $\text{cm}^{-1}$  is caused by the offset of Cd in the Cd ZIF-67 composite [38]. In addition, peaks that can be observed at 120, 413, and 687  $\text{cm}^{-1}$  are evidence for the retention of ZIF-67 [36, 38].

XPS survey spectra of Cd ZIF-67 are shown in Fig. S<sub>3</sub>(A). The spectrum shows that the incorporated elements in the structure are C, N, Co, and Cd, and their atomic abundance percentages are 61.2, 28.3, 4.1, and 6.4%, respectively. The Cd ZIF-67 N 1s core-level spectra are illustrated in Fig. S<sub>3</sub>(B). They are separated into

**Fig. 1** **A** SEM image and **B** SEM image coupled with the EDX elemental mapping distribution of Cd, C, N, and Co elements of Cd ZIF-67

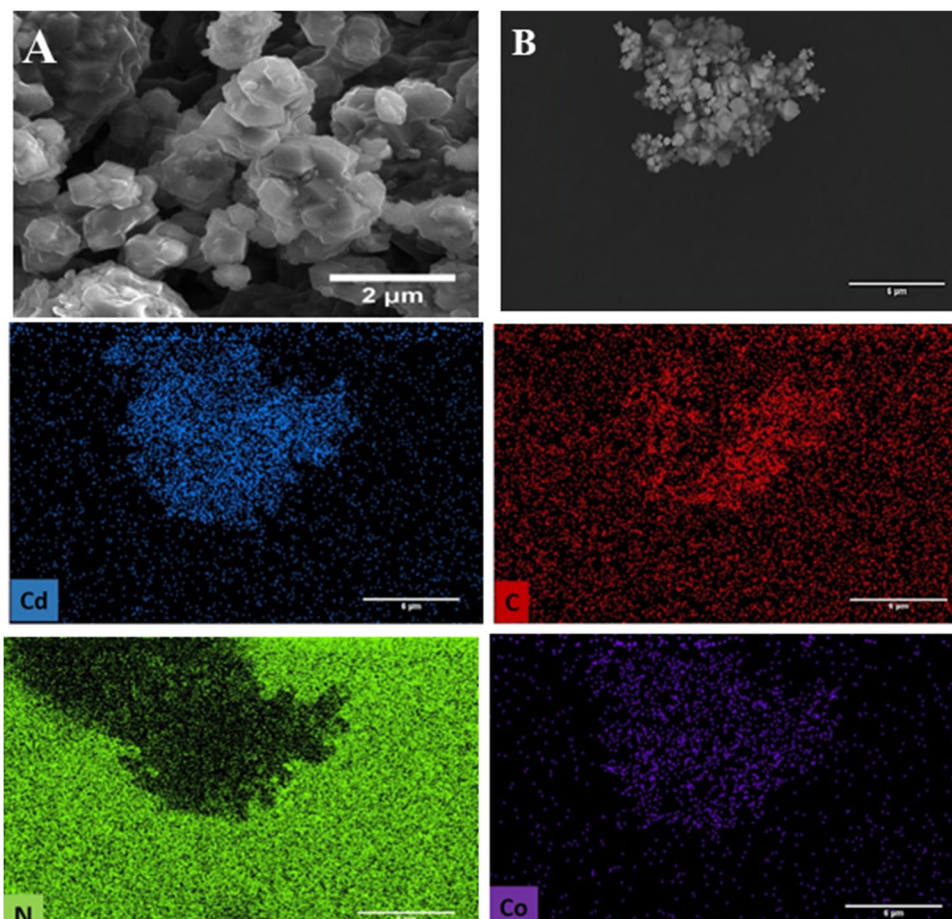
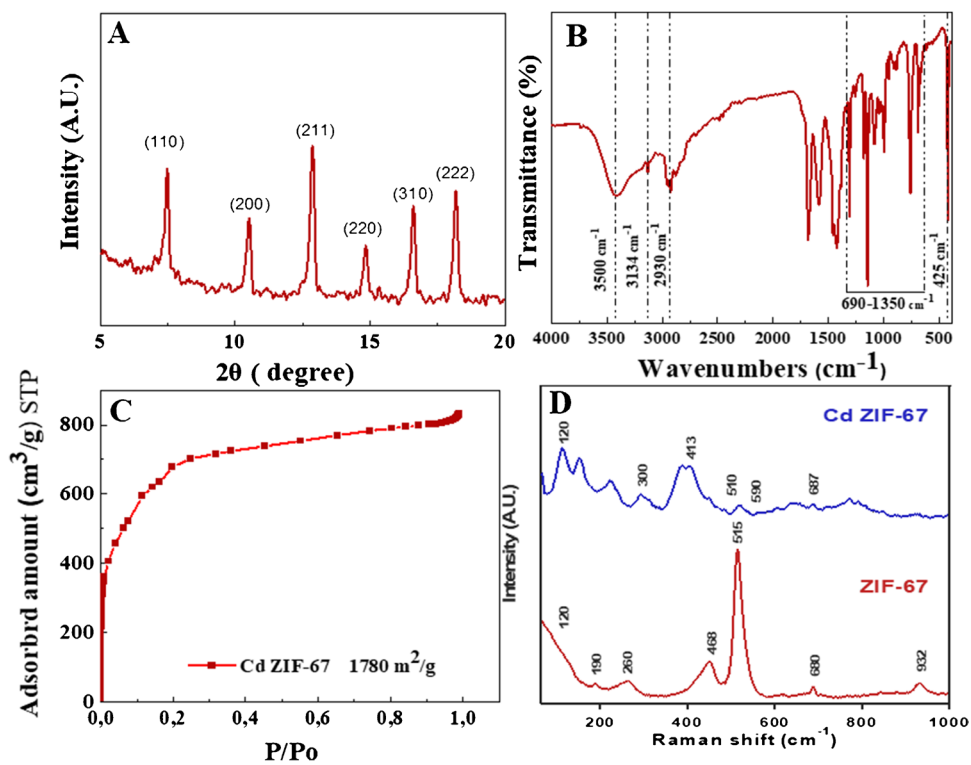


**Fig. 2** **A** PXRD pattern, **B** FTIR, **C** nitrogen sorption measurements at 77 K, and **D** Raman spectra of Cd ZIF-67



several peaks, depending on the nitrogen environment. The deconvolutions were divided into four peaks. The pyridinic nitrogen atoms may be responsible for the strongest N 1 s peaks at 398.8 eV [39]. This peak denotes the successful coordination through nitrogen-sp<sup>2</sup> bonding with metal ions due to the small difference in binding energies between the metal-coordinated N and pyridinic N [40]. It further specifies that most methyl imidazole reactions should result in methyl imidazolate. The deconvoluted C 1 s spectra are shown in Fig.S<sub>3</sub>(C). There are three major peaks at 284.57, 284.99, and 288.15 eV. These peaks may be attributed to the C–C/C=C [41–43], C=N [44–46], and C–N [43, 46, 47], respectively. The Co 2p deconvoluted spectra are shown in Fig.S<sub>3</sub>(D). There are two primary peaks visible. These peaks are indexed to Co 2p<sub>3/2</sub> and 2p<sub>1/2</sub> spin–orbit splitting at 780.9516 and 797.24 eV. The deconvoluting cobalt Co 2p<sub>3/2</sub> and Co 2p<sub>1/2</sub> spectra present two main peaks under each one along with their significant corresponding satellite peaks. The peaks at 782.94, 786.5, and 789.44 eV correspond to the unsaturated Co species in Co–N coordination within the framework [48]. Furthermore, Fig.S<sub>3</sub>(D) shows the XPS spectra of Cd incorporated in Cd ZIF-67, showing two main peaks at 412.37 and 405.21 eV, which are recognized as Cd 3d<sub>3/2</sub> and Cd 3d<sub>5/2</sub>, respectively, representing the Cd<sup>2+</sup> oxidation state [49]. The spin–orbit interaction with Cd(3d<sub>5/2</sub>) and Cd(3d<sub>3/2</sub>) produced the fine doublet at energies of 406.51 and 411.85 eV, respectively [50].

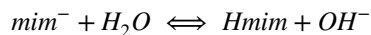
### Electrochemical characterization of as-prepared sensors

Previous studies [51, 52] indicated that metal nanoparticles co-formulated with modified electrode materials rarely undergo oxidation in aqueous buffer solutions [52], except [53, 54] when they are exposed to a strongly acidic medium of 0.5 M HCl (pH 0.3) [53]. The electrochemical behavior of the GCS<sub>2</sub> was first studied by cyclic voltammetry to prove the incorporation of Cd in ZIF-67. Cyclic voltammograms for both BGCS and GCS<sub>2</sub> were recorded in a 0.5 M HCl solution (Fig.S<sub>4</sub>). The electrochemical response for BGCS (red line, curve a) shows no redox processes; however, the GCS<sub>2</sub> (blue line, curve b) showed a characteristic oxidation process at –898 mV and a reduction process at –982 mV in the reverse scan for the Cd redox process.

### Electroactive surface area and resistive properties

ZIF-67 usually has a positive surface charge [55, 56]. Nafion, a negatively charged perfluorinated polymer, can

bind to positively charged ZIF-67 and form a stable porous film on electrode surfaces. This agrees with the results of the point of zero charges previously mentioned. As previously reported, contacting ZIF-67 with water could result in a pH increase, which might be due to the protonation effect of imidazolate groups (mim) exposed at the outer surface of the ZIF-67 particles [57], according to the equation:



The interactions between anionic species and ZIF-67, which has a positive surface charge, were made easier by the solution's increased pH. Furthermore, the uncoordinated Co<sup>2+</sup> sites at the outer surface of ZIF-67 were deemed to bond with hydroxide derived from water in an aqueous solution [58]. This means that ZIF-67 could adsorb anionic [Fe(CN)<sub>6</sub>]<sup>3–/4–</sup> species through electrostatic interactions.

The electroactive surface area of bare and modified stripping voltammetric glassy carbon sensors was measured to provide more information about the electrochemical properties of the surface of BGCS and as-prepared sensors. Figure 3A demonstrates the CV of 10 mM K<sub>3</sub>[Fe(CN)<sub>6</sub>] in 0.1 M of KCl as a redox probe cell system using BGCS and GCS<sub>1–3</sub> sensors (scan rate (*v*) of 100 mV·s<sup>–1</sup>). The CV voltammograms demonstrate a well-defined redox peak, owing to the reversible electron transfer rate of [Fe(CN)<sub>6</sub>]<sup>3–/4–</sup> compared to unmodified GCS. Moreover, the redox peaks display Δ*E*<sub>p</sub> values almost equal to 140, 100, and 150 mV for the GCS<sub>1</sub>, GCS<sub>2</sub>, and GCS<sub>3</sub> sensors, respectively, compared to the BGCS (Δ*E*<sub>p</sub> = 210 mV).

Notably, the amount of charges on the as-prepared sensors' surface causes an acceleration of the rate of electron transfer of [Fe(CN)<sub>6</sub>]<sup>3–/4–</sup> on the as-prepared sensors' surface, which accounts for the Δ*E*<sub>p</sub> values decreasing for some of the as-prepared sensors. Furthermore, [Fe(CN)<sub>6</sub>]<sup>3–/4–</sup> had its highest redox peak current intensity at the GCS<sub>2</sub> sensor, which may be due to the large surface area of Cd ZIF-67, and the good conductivity of co-mixed metal ions (Co and Cd).

By using the Randles–Sevcik equation [59], the electroactive surface area (*A*<sub>surface</sub>) of all as-prepared sensors was evaluated from *i*<sub>p</sub> versus *v*<sup>1/2</sup> plots relating the CV of 10 mM of K<sub>4</sub>[Fe(CN)<sub>6</sub>] in 0.1 M of KCl at *v* ≈ 20–400 mV·s<sup>–1</sup> (Fig. S<sub>5</sub> and Fig. 3B) according to the following equation:

$$i_p = (2.69 \times 10^5) n^{3/2} A_{\text{surface}} D^{1/2} v^{1/2}$$

where *n* is the amount of e<sup>–</sup> in the electrochemical process, *D* is the diffusion coefficient (7.6 μm<sup>2</sup>·s<sup>–1</sup>), *A*<sub>surface</sub> is the electroactive surface area of the as-prepared sensor, and *C* is the concentration of K<sub>3</sub>[Fe(CN)<sub>6</sub>]. The values of the electroactive area of BGCS and GCS<sub>1–3</sub> sensors were calculated to be 0.056, 0.13, 0.21, and 0.11 cm<sup>2</sup>, respectively. It is noteworthy that the GCS<sub>2</sub> sensor has the highest *A*<sub>surface</sub> value, with a fourfold increase compared to the BGCS.

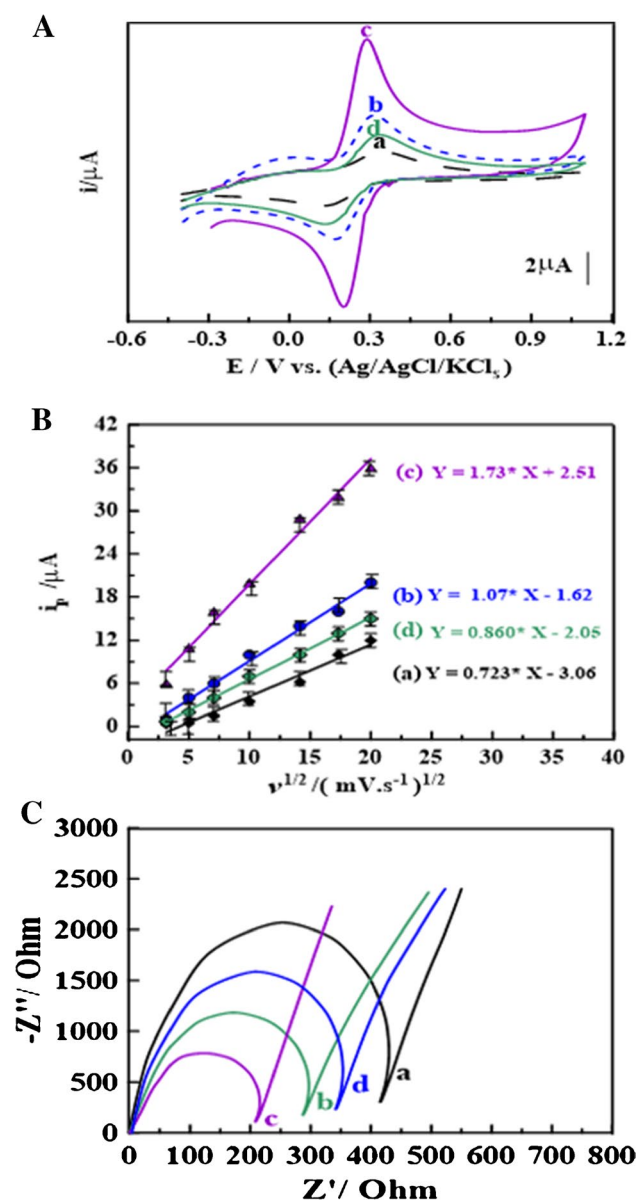


**Fig. 3** **A** CVs of 10 mM of  $K_3[Fe(CN)_6]$  in 0.1 M of KCl ( $v=100 \text{ mV}\cdot\text{s}^{-1}$ ), and **B** plot of  $i_p$  vs.  $v^{1/2}$  relating CVs at  $v \approx 10\text{--}400 \text{ mV}\cdot\text{s}^{-1}$  using (a) BGCS and (b) GCS<sub>1</sub>, (c) GCS<sub>2</sub>, and (d) GCS<sub>3</sub> sensors ( $n=3$ ). **C** Nyquist plots of 10.0 mM  $K_3[Fe(CN)_6]$  in 0.1 M of KCl utilizing (a) BGCS, (b) GCS<sub>1</sub>, (c) GCS<sub>2</sub>, and (d) GCS<sub>3</sub> sensors ( $n=3$ )

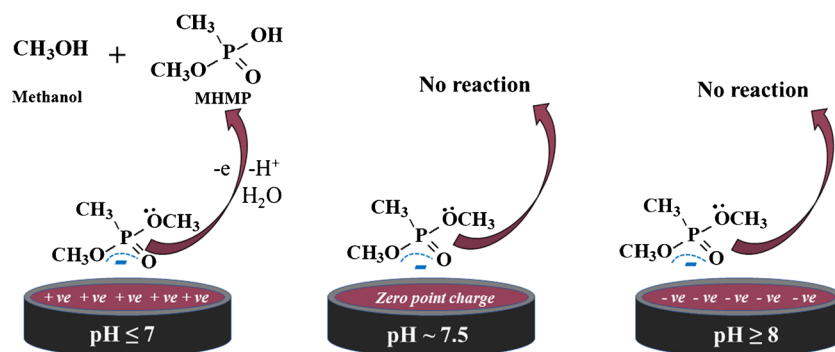
Furthermore, the charge transfer resistance ( $R_{ct}$ ) at the interface of BGCS and as-prepared sensors was accounted for via electrochemical impedance spectroscopy (EIS) [60]. Nyquist plots for BGCS and GCS<sub>1-3</sub> sensors were measured in 0.1 M of KCl containing 10.0 mM  $K_3[Fe(CN)_6]$  to provide more details about the performance of the sensing mechanism of all as-prepared sensors (Fig. 3C).  $R_{ct}$  values were evaluated to be  $420 \pm 1.53$ ,  $290 \pm 2.51$ ,  $200 \pm 2.08$ , and  $330 \pm 2.08 \Omega$  for the BGCS and GCS<sub>1-3</sub> sensors, respectively.

The GCS<sub>2</sub> exhibited a development in the rate of electron transfer with low resistivity compared to the BGCS and all other as-prepared sensors.

### Electrochemical behavior and sensor reaction mechanism of DMMP

To clarify the electrochemical behavior of DMMP, cyclic voltammograms (CVs) of 1.0  $\mu\text{M}$  DMMP were measured in B-R universal buffer of different pH values upon the surface of GCS<sub>2</sub> at scan rate ( $v=100 \text{ mV}\cdot\text{s}^{-1}$ ). As displayed in Fig. S<sub>6</sub>, the CV of DMMP in pH 4 displayed the main oxidation peak at peak potential ( $E_p$ )  $\approx -0.75 \text{ V}$ , which could be related to the selective oxidation of the phosphonate group into phosphate [61, 62]. The voltammogram did not show the oxidation/reduction couple for Cd in the sensor material, which means that Cd nanoparticles in the sensor material are electrochemically inert in the investigated B-R buffer solutions. No anodic peak was observed in the reverse scan upon increasing the scan rate from 10 to 500 mV/s suggesting that the oxidation reaction of DMMP can be chemically irreversible electron transfer for the scan rates being used, in which the redox event is followed by a chemical reaction (EC mechanism) [63]. On the other side, it was observed that  $E_p$  shifts linearly in negative direction with an increase in pH, following the equation:  $E_p \text{ (V)} = (-0.067 \pm 0.0022) \text{ pH} + (0.45 \pm 0.031)$  ( $R^2 = 0.998$  and  $n=6$ ) (pH of 2.0–7.0), as shown in Fig. S<sub>7</sub>(B), which indicates the involvement of protons in the electrochemical oxidation of DMMP at the surface of GCS<sub>2</sub>. Generally, the number of protons participating in the electrochemical reaction was calculated for the reversible or quasi-reversible electrode reaction process [64]. This slope value of 0.067 V/pH was close to the Nernst slope of 0.059 V/pH at 25 °C. This result indicated that an equal number of protons and electrons took part in the oxidation process of DMMP [65]. Furthermore, the transfer coefficient ( $\alpha$ ) was evaluated to be 0.73 while assuming the number of electrons ( $n_a$ ) is equal to 1 from the slope value of the linear plot of  $E_p$  vs.  $\ln v$  of 1.0  $\mu\text{M}$  DMMP in B-R universal buffer (pH 4) using GCS<sub>2</sub> (Fig. S<sub>7</sub>(C)), which is expressed by the following equation [66]:  $E_p \text{ (V)} = (0.035 \pm 0.0037) \ln v \text{ (mV}\cdot\text{s}^{-1}) + (0.880 \pm 0.045)$  ( $R^2 \approx 0.984$  and  $n=8$ ). As for a completely irreversible and reversible electrode reaction,  $\alpha$  can be taken as 0.5 and 1.0, respectively [67]; the electrode reaction can be considered a quasi-reversible reaction for the scan rates being considered (10–500 mV/s). Further,  $[\Delta E = E_p - E_{p/2}]$  of 55 to 60 mV suggested also the quasi-reversible electrode process. For such a quasi-reversible system [68, 69],  $[E_p - E_{p/2}] = 1.857 RT/(an_a F)$ , values of  $an_a$  (0.80–0.87) were also calculated at various pH values. These results confirm the participation of an equal number of protons ( $p$ ) and electron transfer ( $n_a$ ), which is assumed to be 1 in the oxidation mechanism [70], as demonstrated

**Scheme 1** The proposed mechanism for the oxidation of DMMP



in Scheme 1. As well, the linear plot of  $\text{Log } i_p$  vs.  $\text{Log } \nu$  in a B-R buffer  $pH$  4 was estimated to investigate the adsorption-controlled process of the DMMP upon the surface of  $\text{GCS}_2$ , which is expressed by the following equation:  $\text{Log } i_{p/\mu\text{A}} = (1.023 \pm 0.004) \text{Log } \nu_{\text{mV.s}}^{-1} - (1.84 \pm 0.033)$  ( $n=8$  and  $R^2 = 0.998$ ), as displayed in Fig.S<sub>7</sub>(D). The obtained slope value suggests that the oxidation process of the DMMP on the surface of  $\text{GCS}_2$  is controlled by the adsorption process [18].

The anodic/forward charge transfer may be followed by a homogenous irreversible chemical reaction [63, 71]. The product of electron transfer from the oxidation process has been chemically consumed in the formation of the follow-up product and is therefore not available for reduction at such a low scan rate (i.e., at this time-scale of the experiment, the backward electron transfer reaction could not take place, leaving the forward reaction dominant) [63, 71]. Adsorption effects may also contribute to the absence of the peak in the reverse direction [72]. Samin et al. observed similar results [72] which successfully captured the physics with a model taking into account diffusion, kinetics, adsorption effects, and morphology changes on the electrode surface or the electron transfer step.

As suggested in mechanism (Scheme 1), the methoxy group (O-CH<sub>3</sub>) and phosphoryl oxygen (P=O) of DMMP were linked with the surface of  $\text{GCS}_2$  with an electrostatic attraction force depending on the Lewis acid–base interactions [73]. The methoxy group (O-CH<sub>3</sub>) is first cleaved and protonated to generate methanol (CH<sub>3</sub>OH) as a by-product, accompanied by the formation of methyl hydrogen methyl phosphonate (MHMP) molecules [74, 75]. As shown in Fig.S<sub>7</sub>(A), the  $i_p$  vs.  $pH$  plot confirmed that the highest  $i_p$  was obtained at  $pH$  4, followed by a gradual decrease with increasing  $pH$  until complete disappearance at  $pH > 8$ . This electrochemical performance may arise from the electrostatic repulsion between DMMP and  $\text{GCS}_2$ , which can be further explained by the following reasons: As stated previously, the charge delocalization throughout the solvated DMMP was measured and displayed with a  $-ve$  charge ( $-1.8858431$ ) using the Gaussian 09 program package. At  $pH \leq 3.0$ , the magnitude of  $i_p$  is very small, owing to

the repulsion force between the strong protonated form of DMMP molecules ( $+ve$ ) in the acidic medium (acid–base dissociation constant ( $pK_a \sim 2.37$  [76])) and the positively charged surface ( $+ve$ ) of  $\text{GCS}_2$  ( $pH_{zpc} \sim 7.3$ ; Fig.S<sub>2</sub>), as shown in Scheme 1. Thus, the mechanism of the reaction mainly depends on the electrostatic attraction force accompanied by the adsorption characteristics between the DMMP molecules and the surface of  $\text{GCS}_2$ , which occur easily at  $pH$  4. At  $pH \geq 8$ , the  $i_p$  is completely disappeared, due to the occupancy of the surface of DMMP and  $\text{GCS}_2$  with a lone pair of electrons upon methoxy groups ( $-ve$ ) and imidazole groups ( $-ve$ ), which hinders the electrostatic attraction between the DMMP molecules and the surface of  $\text{GCS}_2$ .

#### The adsorption behavior and the preliminary stripping voltammetry test of as-prepared sensors

The preliminary anodic stripping voltammetric scan of 2.0  $\mu\text{M}$  of DMMP in the BR buffer  $pH$  4 (Fig.S<sub>8</sub>(A)) was recorded utilizing BGCS,  $\text{GCS}_1$ ,  $\text{GCS}_2$ , and  $\text{GCS}_3$  sensors at an accumulation potential ( $E_{acc}$ ) of  $-1.5$  V (versus Ag/AgCl/KCl<sub>s</sub>) using the square-wave adsorptive anodic stripping voltammetry technique (SW-AdASV) at  $t_{acc} = 30$  s,  $a = 25$  mV,  $f = 100$  Hz, and  $\Delta E_s = 10$  mV. Notably, the  $i_p$  of  $\text{GCS}_2$  displayed a greater affinity for DMMP with about a threefold increase concerning the bare CPS, which may arise from the improvements in the electroactive surface area features of the utilized modifier material.

In this context, the adsorption behavior of the DMMP on the surface of the BGCS (inset; Fig.S<sub>8</sub>(B)) and  $\text{GCS}_2$  (Fig.S<sub>8</sub>(B)) sensors was also evaluated by recording CV voltammograms of 1.0 nM DMMP in the B-R buffer of  $pH$  4. The peak current intensity ( $i_p$ ) voltammograms were recorded without applying adsorptive accumulation time (open circuit conditions) ( $i_{pIII}$ ), followed by utilizing an adsorptive accumulation time of 75 s ( $i_{pI}$  1st cycle and  $i_{pII}$  2nd cycle). According to the adsorptive step, a well-defined peak was noticed at the  $\text{GCS}_2$  ( $i_{pI}$ ; in Fig.S<sub>8</sub>(B)), owing to the great enhancement in the adsorption property toward DMMP even at open circuit conditions ( $i_{pIII}$ ). Moreover, the remarkable decline of the  $i_{pII}$  observed in the 2nd cycle may be due to

the desorption of DMMP from the sensor surface. Based on the last-mentioned findings, we can deduce that GCS<sub>2</sub> has the best affinity toward the determination of DMMP, which could be used in electroanalytical studies due to its good catalytic, adsorptive, and selective properties.

### Optimization of the pH medium and analytical parameters

Because of the ion exchange process between the detected sample and the surface of sensor, the *pH* of solution generally has a significant impact on the *i<sub>p</sub>* signal and the clarity of voltammograms of the detected sample on the surface of as-prepared sensors. Thus, the effect of changing *pH* values of B-R buffer (2–8) as a supporting electrolyte on the *i<sub>p</sub>* signal of 0.7 nM of DMMP was tested at *E<sub>acc</sub>* = −1.5 V (vs. Ag/AgCl-KCl) for 30 s using GCS<sub>2</sub> as displayed in Fig.S<sub>9</sub>. The oxidative *i<sub>p</sub>* signal was strongly affected by changing the acidity of the solution from 2 to 7, followed by the complete disappearance of the *i<sub>p</sub>* at *pH* ≥ 8. The highest oxidative peak was obtained at *pH* 4, which was subsequently utilized for optimizing instrumental operational conditions.

The optimum instrumental operational conditions for the detection of DMMP were pointed out to be *pH* 6, *E<sub>acc</sub>* = −1.5 V, *t<sub>acc</sub>* = 30 s, frequency (*f*) = 90 Hz, pulse amplitude (*a*) = 30 mV, and scan increment ( $\Delta E_s$ ) = 10 mV using GCS<sub>2</sub>, as displayed in Figs.S<sub>10</sub>(A, B, and C). According to the adsorption step, the effect of changing *E<sub>acc</sub>* from −1.7 to −1.3 V (vs. Ag/AgCl-KCl) on the *i<sub>p</sub>* signal of 2.0 pM of DMMP in B-R buffer *pH* 4 was estimated for 30 s using GCS<sub>2</sub>, as displayed in Figs.S<sub>11</sub>(A) and (B).

Also, the effect of changing the *t<sub>acc</sub>* of 0.3 and 0.7 nM of DMMP on the *i<sub>p</sub>* signal was estimated, as displayed in Fig. S<sub>11</sub>(C). According to the last-mentioned results, *E<sub>acc</sub>* = −1.5 V and *t<sub>acc</sub>* at 30 s are the optimum accumulation conditions for the determination of DMMP in B-R buffer of *pH* 4, which are employed for the subsequent electroanalytical measurements.

### The electroanalytical detection of DMMP

#### Limits of quantification (LOQ) and detection (LOD)

Under the chosen analytical conditions, the calibration curve of different concentrations of DMMP showed two linear portions over the ranges of 0.02–2.0 and 2.0–9.0 nM into the B-R buffer of *pH* 4 at the GCS<sub>2</sub> was characterized by SW-AdASV, as displayed in Fig. 4A. The linear regression equations of the last-mentioned calibration plots were expressed as follows:  $i_{p/\mu A} = (6.975 \pm 0.138) C_{DMMP/nM} + (0.0423 \pm 0.0047)$  ( $R^2 = 0.990$ ), and  $i_{p/\mu A} = (1.650 \pm 0.33) C_{DMMP/nM} + (9.8 \pm 0.36)$  ( $R^2 = 0.994$ ) with a limit of detection (LOD)  $\approx$  0.06 pM (sensitivity of

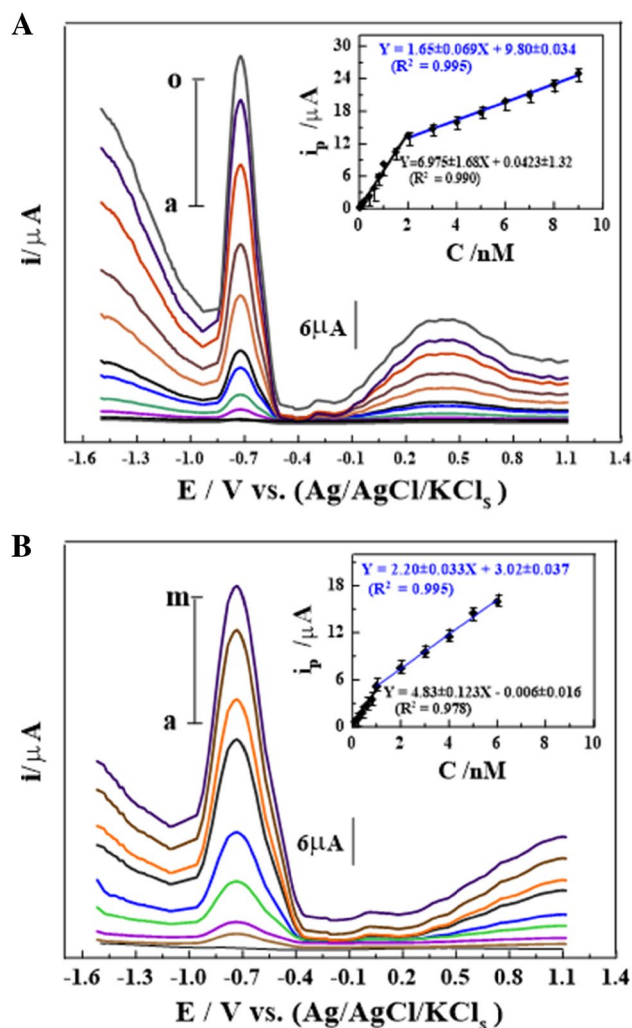


**Fig. 4** A SW-AdAV voltammograms of different amounts of DMMP in *pH* 4 on GCS<sub>2</sub> (*E<sub>acc</sub>* = −1.5 V, *t<sub>acc</sub>* = 60 s,  $\Delta E_s$  = 10 mV, *f* = 90 Hz, and *a* = 30 mV) in bulk form: (a) baseline, (b) 0.04, (c) 0.09, (d) 0.3, (e) 0.6, (f) 0.7, (g) 1.3, (h) 1.7, (m) 5.5, (n) 8.0, and (o) 9.0 nM (inset: its corresponding plot (*n* = 3)). B SW-AdAV voltammograms of different amounts of DMMP in *pH* 4 on GCS<sub>2</sub> (*E<sub>acc</sub>* = −1.5 V, *t<sub>acc</sub>* = 60 s,  $\Delta E_s$  = 10 mV, *f* = 90 Hz, and *a* = 30 mV) in spiked serum form: (a) baseline, (b) 0.1, (c) 0.2, (d) 0.6, (e) 1.0, (f) 3.0, (g) 4.0, (h) 5.0, and (m) 6.0 nM (inset: its corresponding plot (*n* = 3))

6.975  $\mu A/pM$ ). As summarized in Table S1, different types of methods and sensors have been developed to detect DMMP in gaseous and liquid states. Among the mentioned findings in Table S1, we can conclude that GCS<sub>2</sub> has the lowest LOD value and wider linearity range (LR) toward the detection of DMMP in bulk and biological fluid (serum sample) at room temperature (RT) compared to the other reported analytical methods to date. Furthermore, there are no detailed reports on the usage of the SW-AdASV technique for the detection of DMMP in bulk and biological fluids.



## Validity of the as-modified sensor

Under optimum conditions, reliability and repeatability could be evaluated throughout the day (intra-day analysis) and every day over 3 days (inter-day analysis) by recording SW-AdAS voltammograms of 0.3 nM DMMP using five freshly as-modified GCS<sub>2</sub> in parallel. The recovery  $\pm$  relative standard deviation (R%  $\pm$  RSD) of the intra-day and inter-day analysis of DMMP were 101.51%  $\pm$  3.28 and 99.3%  $\pm$  3.36, respectively, revealing the excellent reliability and repeatability of the as-modified sensor. Furthermore, the stability of the as-modified sensor has been checked three times ( $n=3$ ) every 7 days through its storage in air for 30 days at RT, maintaining 96.36% of its initial activity for more than 15 days and reaching 92.3% after 30 days, as figured out in Fig.S<sub>12</sub>(A). As tabulated in Table.S<sub>2</sub>, the results proved that the sensor exhibited proper reliability, repeatability, and long-term stability, owing to the chemical stability of the as-prepared Cd ZIF-67 modifier.

## Selectivity

The anti-interference performance (selectivity) of the GCS<sub>2</sub> was investigated by the addition of common interferences in human biological systems, as displayed in Fig.S<sub>12</sub>(B). The  $i_p$  voltammogram of 0.3 nM of DMMP ( $C_I$ ) (Fig. S<sub>11</sub>(B); a) was evaluated after addition of 30.0 nM ( $\sim$  100-fold) of common metal cations (Mix<sub>1</sub>: Ca<sup>2+</sup>, Mg<sup>2+</sup>, Fe<sup>2+</sup>, Zn<sup>2+</sup>, Co<sup>2+</sup>, Na<sup>+</sup>, and K<sup>+</sup>) and 30.0 nM (100-fold) mixture of S-containing amino acids (S-amino: cysteine (Cys) and thiamine (TA)), as demonstrated in Fig.S<sub>12</sub>(B); b. Noteworthy, there was no noticeable difference in the magnitude of the  $i_p$  voltammogram of 0.3 nM of DMMP with an RSD of 2.88%, and no additional peaks of Mix<sub>1</sub> and S-amino interferences appeared. Moreover, Fig.S<sub>12</sub>(B); c exhibits a new peak at 0.36 V ( $C_{II}$ ), which corresponds to 0.03 nM (15-fold) uric acid (UA) with a relative error (RE %)  $\sim \pm 1.2$  at the DMMP peak. Furthermore, Fig.S<sub>12</sub>(B); d demonstrates another peak at 0.15 V ( $C_{III}$ ) after the addition of 30.0 nM ( $\sim$  100-fold) of the mixture of other interferences (Mix<sub>2</sub>: ascorbic acid (AA), dopamine (DA), and glucose (Glu.)).

On the other hand, the specificity performance of the GCS<sub>2</sub> was investigated toward the detection of DMMP in the presence of compounds with similar electroactive functional groups such as glyphosate (GLYP) and chlorpyrifos (CPYP) in bulk form, as displayed in Scheme.S<sub>1</sub> and Fig.S<sub>13</sub>. The  $i_p$  voltammogram of 0.6 nM of DMMP (Fig. S<sub>12</sub>; a) was evaluated with the same value even after the addition of 60.0 nM of GLYP, which demonstrated a small peak at  $-0.02$  V, corresponding to (GLYP). According to previous reports by Wu et al. [44], Indra et al. [45], and Liu et al. [46], the limitation in the detection response of GLYP during the detection of DMMP could arise from the usage of an optimized

pH medium (universal buffer; pH 4), which is far from the reported optimized pH condition (phosphate buffer; pH 7) in the detection of GLYP. Moreover, the  $i_p$  voltammogram of 0.6 nM of DMMP did not show any additional oxidation peak associated with the addition of 60.0 nM of CPYP as a result of it not being oxidized (Fig. S<sub>13</sub>; b) [47]. These results proved that the presence of common interferences in human biological systems and other compounds with the same electroactive functional groups does not interfere with the detection of DMMP, even when the concentrations exceed 100-fold.

## Application in spiked human serum fluid

The GCS<sub>2</sub> was applied to detect DMMP, spiked in human serum samples of 3 healthy volunteers in the B-R buffer of pH 4 using SW-AdASV under the chosen analytical conditions without the necessity for sample pre-treatment steps. SW-AdAS voltammograms of different concentrations of DMMP in the presence of spiked human serum samples (Voulanter<sub>1</sub>) over two linear ranges of 0.1–1.0 and 1.0–6.0 nM into the B-R buffer of pH 4 at the GCS<sub>2</sub> with a LOD  $\approx$  0.03 nM (sensitivity of 4.83  $\mu$ A/nM), as displayed in Fig. 4B. Moreover, 0.6 and 1.0 nM of DMMP were estimated in the presence of spiked human serum samples (Voulanter<sub>2,3</sub>), which achieved a good recovery (R %)  $\pm$  relative standard deviation (RSD %) without interference from other biological contents, as summarized in Table.S<sub>3</sub>. These results proved that the fabricated sensor exhibited proper accuracy (RE %) and reliability in the detection of DMMP even among complex biological systems.

## Conclusion

This work involved the successful hydrothermal synthesis of porous nanoparticles of Cd ZIF-67 with a rhombic dodecahedral morphology, which were then applied to the construction of an electrochemical sensor for DMMP. The porous Cd ZIF-67 nanoparticles possessed a high surface area, while 1.0% of the modified GCS (GCS<sub>2</sub>) promoted the electrocatalytic activity and adsorption behaviors of BGCS. Subsequently, the GCS<sub>2</sub> exhibited low limit of detection in bulk with proper reliability, long-term stability, and repeatability, which were necessary for the electroanalytical detection. Furthermore, the fabricated modified sensor exhibited a proper accuracy and reliability in the detection of DMMP even among complex biological systems.

**Supplementary Information** The online version contains supplementary material available at <https://doi.org/10.1007/s00604-023-06112-3>.

**Funding** Open access funding provided by The Science, Technology & Innovation Funding Authority (STDF) in cooperation with The Egyptian Knowledge Bank (EKB).

**Data availability** Data available on request from the authors.

## Declarations

**Conflict of interest** The authors declare no competing interests.

**Open Access** This article is licensed under a Creative Commons Attribution 4.0 International License, which permits use, sharing, adaptation, distribution and reproduction in any medium or format, as long as you give appropriate credit to the original author(s) and the source, provide a link to the Creative Commons licence, and indicate if changes were made. The images or other third party material in this article are included in the article's Creative Commons licence, unless indicated otherwise in a credit line to the material. If material is not included in the article's Creative Commons licence and your intended use is not permitted by statutory regulation or exceeds the permitted use, you will need to obtain permission directly from the copyright holder. To view a copy of this licence, visit <http://creativecommons.org/licenses/by/4.0/>.

## References

- Chauhan S, D'cruz R, Faruqi S, Singh K, Varma S, Singh M, Karthik V (2008) Chemical warfare agents. *Environ Toxicol Pharmacol* 26:113–122. <https://doi.org/10.1016/j.etap.2008.03.003>
- Mercey G, Verdelet T, Renou J, Kliachyna M, Baati R, Nachon F, Jean L, Renard P-Y (2012) Reactivators of acetylcholinesterase inhibited by organophosphorus nerve agents. *Acc Chem Res* 45(5):756–766. <https://doi.org/10.1021/ar2002864>
- S. Mukherjee, R. Gupta, (2020) Organophosphorus nerve agents: types, toxicity, and treatments, 2020. <https://doi.org/10.1155/2020/3007984>
- Yoo R, Cho S, Song M-J, Lee WJS (2015) Highly sensitive gas sensor based on Al-doped ZnO nanoparticles for detection of dimethyl methylphosphonate as a chemical warfare agent simulant. *Sens Actuators, B Chem* 221:217–223. <https://doi.org/10.1016/j.snb.2015.06.076>
- Lee SC, Choi HY, Lee SJ, Lee WS, Huh JS, Lee DD, Kim JC (2009) The development of SnO<sub>2</sub>-based recoverable gas sensors for the detection of DMMP. *Sens Actuators, B Chem* 137(1):239–245. <https://doi.org/10.1016/j.snb.2008.12.051>
- Lee SC, Kim SY, Lee WS, Jung SY, Hwang BW, Ragupathy D, Lee DD, Lee SY, Kim JC (2011) Effects of textural properties on the response of a SnO<sub>2</sub>-based gas sensor for the detection of chemical warfare agents. *Sensors* 11(7):6893–6904. <https://doi.org/10.3390/s110706893>
- K-H Yun, K-Y Yun, G-Y Cha, BH Lee, JC Kim, D-D Lee, JS Huh (2005) Gas sensing characteristics of ZnO-doped SnO<sub>2</sub> sensors for simulants of the chemical agents. In *Materials science forum* Vol. 486: 9–12. Trans Tech Publications Ltd. <https://doi.org/10.4028/www.scientific.net/MSF.486-487.9>
- Kim H-C, Hong S-H, Kim S-J, Lee J-H (2011) Effects of additives on the DMMP sensing behavior of SnO<sub>2</sub> nanoparticles synthesized by hydrothermal method. *J Sensor Sci Technol* 20(5):294–299. <https://doi.org/10.5369/JSS.2011.20.5.294>
- Yoo R, Yoo S, Lee D, Kim J, Cho S, Lee W (2017) Highly selective detection of dimethyl methylphosphonate (DMMP) using CuO nanoparticles/ZnO flowers heterojunction. *Sens Actuators, B Chem* 240:1099–1105. <https://doi.org/10.1016/j.snb.2016.09.028>
- Dipak P, Samadhiya A, Kumar N, Singh PA, Tiwari DC, Verma UP (2022) Fabrication of fast response and recovery NiFeAl<sup>3+</sup> nanocomposite gas sensor for detection of dimethyl methyl phosphonate. *J Electron Mater* 51(8):4456–4464. <https://doi.org/10.1007/s11664-022-09700-w>
- Sharma PK, Gupta G, Singh VV, Tripathi B, Pandey P, Boopathi M, Singh B, Vijayaraghavan R (2010) Synthesis and characterization of polypyrrole by cyclic voltammetry at different scan rate and its use in electrochemical reduction of the simulant of nerve agents. *Synth Met* 160(23–24):2631–2637. <https://doi.org/10.1016/j.synthmet.2010.10.016>
- Mukherjee A, Dunayevskiy I, Prasanna M, Go R, Tsekoun A, Wang X, Fan J, Patel CKN (2008) Sub-parts-per-billion level detection of dimethyl methyl phosphonate (DMMP) by quantum cascade laser photoacoustic spectroscopy. *Appl Opt* 47(10):1543–1548. <https://doi.org/10.1364/AO.47.001543>
- Alev O, Özdemir O, Goldenberg E, Arslan LÇ, Büyükköse S, Öztürk ZZJTSF (2022) WS<sub>2</sub> thin film based quartz crystal microbalance gas sensor for dimethyl methylphosphonate detection at room temperature. *Thin Solid Films* 745:139097. <https://doi.org/10.1016/j.tsf.2022.139097>
- Shaik M, Rao VK, Ramana G, Halder M, Gutch P, Pandey P, Jain R (2018) p-Hexafluoroisopropanol phenyl functionalized graphene for QCM based detection of dimethyl methylphosphonate, a simulant of the nerve agent sarin. *RSC Adv* 8(15):8240–8245. <https://doi.org/10.1039/C7RA12272A>
- Asadi S, Maddah B (2022) Rapid screening of chemical warfare agents (nerve agents) using dimethyl methylphosphonate as simulant substances in beverages by hollow fiber membrane-protected solid phase microextraction followed by corona discharge ion mobility spectrometry. *J Chromatogr A* 1661:462704. <https://doi.org/10.1016/j.chroma.2021.462704>
- McKenna J, Dhummakupt ES, Connell T, Demond PS, Miller DB, Nilles JM, Manicke NE, Glaros TJA (2017) Detection of chemical warfare agent simulants and hydrolysis products in biological samples by paper spray mass spectrometry. *Analyst* 142(9):1442–1451. <https://doi.org/10.1039/C7AN00144D>
- Yang X, Chen S, Zhang H, Huang Z, Liu X, Cheng Z, Li T (2020) Trace level analysis of nerve agent simulant DMMP with silicon nanowire FET sensor. *IEEE Sens J* 20(20):12096–12101. <https://doi.org/10.1109/JSEN.2020.2999378>
- Elfiky M, Beltagi AM, Abuzalat O (2021) Selective modified stripping voltammetric sensor based on Ce-1, 4-benzenedicarboxylic metal-organic frameworks porous nanoparticles for picomolar detection of curcumin. *J Electroanal Chem* 898:115606. <https://doi.org/10.1016/j.jelechem.2021.115606>
- Rowell JL, Yaghi OM (2004) Metal-organic frameworks: a new class of porous materials. *Microporous Mesoporous Mater* 73(1–2):3–14. <https://doi.org/10.1016/j.micromeso.2004.03.034>
- Kitagawa S, Kitaura R, Noro SI (2004) Functional porous coordination polymers. *Angew Chem Int Ed* 43(18):2334–2375. <https://doi.org/10.1002/anie.200300610>
- Zhang J, Tan Y, Song W-J (2020) Zeolitic imidazolate frameworks for use in electrochemical and optical chemical sensing and biosensing: a review. *Microchim Acta* 187:1–23. <https://doi.org/10.1007/s00604-020-4173-3>
- Dong Y, Duan C, Sheng Q, Zheng J (2019) Preparation of Ag@ zeolitic imidazolate framework-67 at room temperature for electrochemical sensing of hydrogen peroxide. *Analyst* 144(2):521–529. <https://doi.org/10.1039/C8AN01641K>
- DMello ME, Sundaram NG, Kalidindi SB (2018) Assembly of ZIF-67 metal-organic framework over tin oxide nanoparticles for synergistic chemiresistive CO<sub>2</sub> gas sensing. *Chemistry-A European J* 24(37):9220–9223
- Kim K, Kim J, Bae Y-S, Engineering (2022) Zn-Co bimetallic zeolitic imidazolate frameworks as nonenzymatic

- electrochemical glucose sensors with enhanced sensitivity and chemical stability. *ACS Sustainable Chemistry & Engineering* 10(35):11702–11709. <https://doi.org/10.1021/acsschemeng.2c04306>
25. Yang N, Zhou X, Qi X, Li J, Fang W, Xue H, Yang Z (2022) A nitrite sensor based on bimetallic zeolitic imidazole framework derived Co/porous carbon nanorods. *Microchem J* 182:107910. <https://doi.org/10.1016/j.microc.2022.107910>
26. Zareba JK, Nyk M, Samoc M (2016) Co/ZIF-8 heterometallic nanoparticles: control of nanocrystal size and properties by a mixed-metal approach. *Cryst Growth Des* 16(11):6419–6425. <https://doi.org/10.1021/acs.cgd.6b01090>
27. Sun W, Zhai X, Zhao L (2016) Co/ZIF-8 heterometallic nanoparticles: control of nanocrystal size and properties by a mixed-metal approach. *Cryst Growth Des* 16(11):6419–6425. <https://doi.org/10.1021/acs.cgd.6b01090>
28. Nordin N, Ismail A, Mustafa A, Goh P, Rana D, Matsuura T (2014) Aqueous room temperature synthesis of zeolitic imidazole framework 8 (ZIF-8) with various concentrations of triethylamine. *RSC Adv* 4(63):33292–33300. <https://doi.org/10.1039/C4RA03593C>
29. Pan Y, Liu Y, Zeng G, Zhao L, Lai Z (2011) Rapid synthesis of zeolitic imidazolate framework-8 (ZIF-8) nanocrystals in an aqueous system. *Chem Commun* 47(7):2071–2073. <https://doi.org/10.1039/C0CC05002D>
30. P. Scherrer (1912) Bestimmung der inneren Struktur und der Größe von Kolloidteilchen mittels Röntgenstrahlen. *Kolloidchemie Ein Lehrbuch* 387–409. [https://doi.org/10.1007/978-3-662-33915-2\\_7](https://doi.org/10.1007/978-3-662-33915-2_7)
31. Prathap MUA, Gunasekaran S (2018) Rapid and scalable synthesis of zeolitic imidazole framework (ZIF-8) and its use for the detection of trace levels of nitroaromatic explosives. *Adv Sustain Syst* 2(10):1800053. <https://doi.org/10.1002/adsu.201800053>
32. Kaur H, Mohanta GC, Gupta V, Kukkar D, Tyagi S (2017) Synthesis and characterization of ZIF-8 nanoparticles for controlled release of 6-mercaptopurine drug. *J Drug Deliv Sci Technol* 41:106–112. <https://doi.org/10.1016/j.jddst.2017.07.004>
33. Schejn A, Balan L, Falk V, Aranda L, Medjahdi G, Schneider R (2014) Controlling ZIF-8 nano- and microcrystal formation and reactivity through zinc salt variations. *CrystEngComm* 16(21):4493–4500. <https://doi.org/10.1039/C3CE42485E>
34. Liu J, He J, Wang L, Li R, Chen P, Rao X, Deng L, Rong L, Lei J (2016) NiO-PTA supported on ZIF-8 as a highly effective catalyst for hydrocracking of Jatropha oil. *Sci Rep* 6(1):23667. [https://doi.org/10.1038/srep23667\(2016\)](https://doi.org/10.1038/srep23667(2016))
35. Hillman F, Zimmerman JM, Paek S-M, Hamid MR, Lim WT, Jeong H-K (2017) Rapid microwave-assisted synthesis of hybrid zeolitic-imidazolate frameworks with mixed metals and mixed linkers. *J Mater Chem A* 5(13):6090–6099. <https://doi.org/10.1039/C6TA11170J>
36. Zhao K, Li H, Tian S, Yang W, Wang X, Pang A, Xie C, Zeng D (2019) A facile low-temperature synthesis of hierarchical porous Co<sub>3</sub>O<sub>4</sub> micro/nano structures derived from ZIF-67 assisted by ammonium perchlorate. *Inorganic Chemistry Frontiers* 6(3):715–722. <https://doi.org/10.1039/C8QI01279B>
37. Hasan Z, Cho D-W, Chon C-M, Yoon K, Song H (2016) Reduction of p-nitrophenol by magnetic Co-carbon composites derived from metal organic frameworks. *Chem Eng J* 298:183–190. <https://doi.org/10.1016/j.cej.2016.04.029>
38. Król M, Koleżyński A, Mozgawa W (2021) Vibrational spectra of zeolite Y as a function of ion exchange. *Molecules* 26(2):342. <https://doi.org/10.3390/molecules26020342>
39. Chen H, Wu X, Zhao R, Zheng Z, Yuan Q, Dong Z, Gan W (2019) Preparation of reduced graphite oxide loaded with cobalt (II) and nitrogen co-doped carbon polyhedrons from a metal-organic framework (type ZIF-67), and its application to electrochemical determination of metronidazole. *Microchim Acta* 186:1–9. <https://doi.org/10.1007/s00604-019-3737-6>
40. Abuzalat O, Tantawy H, Basuni M, Alkordi MH, Baraka A (2022) Designing bimetallic zeolitic imidazolate frameworks (ZIFs) for aqueous catalysis: Co/Zn-ZIF-8 as a cyclic-durable catalyst for hydrogen peroxide oxidative decomposition of organic dyes in water. *RSC Adv* 12(10):6025–6036. <https://doi.org/10.1039/D2RA00218C>
41. OnáChan HS, MingáGan L, HaráChew C, HowáSeow S (1993) Characterization of chemically and electrochemically prepared polyanilines in inverse microemulsions. *J Mater Chem* 3(11):1109–1115. <https://doi.org/10.1039/JM9930301109>
42. Lee H, Choi YN, Choi SB, Seo JH, Kim J, Cho IH, Gang S, Jeon CH (2014) In situ neutron powder diffraction and X-ray photoelectron spectroscopy analyses on the hydrogenation of MOF-5 by Pt-doped multiwalled carbon nanotubes. *J Phys Chem C* 118(11):5691–5699. <https://doi.org/10.1021/jp411955y>
43. Xu L, Meng F, Wei X, Lin C, Zheng L, Liu J (2020) Large-scale multirole Zn (II) programmed synthesis of ultrathin hierarchically porous carbon nanosheets. *Sci China Technol Sci* 63:1730–1738. <https://doi.org/10.1007/s11431-019-1510-0>
44. Wu Y, Song X, Xu S, Zhang J, Zhu Y, Gao L, Xiao G (2019) 2-Methylimidazole modified Co-BTC MOF as an efficient catalyst for chemical fixation of carbon dioxide. *Catal Lett* 149:2575–2585. <https://doi.org/10.1007/s10562-019-02874-9>
45. Indra A, Menezes PW, Kailasam K, Hollmann D, Schröder M, Thomas A, Brückner A, Driess M (2016) Nickel as a co-catalyst for photocatalytic hydrogen evolution on graphitic-carbon nitride (sg-CN): what is the nature of the active species? *Chem Commun* 52(1):104–107. <https://doi.org/10.1039/C5CC07936E>
46. Liu H, Li Z, Zhang L, Ruan H, Hu R (2019) MOF-derived ZnSe/N-doped carbon composites for lithium-ion batteries with enhanced capacity and cycling life. *Nanoscale Res Lett* 14:1–10. <https://doi.org/10.1186/s11671-019-3055-2>
47. Yin B, Cao X, Pan A, Luo Z, Dinesh S, Lin J, Tang Y, Liang S, Cao G (2018) Encapsulation of CoS<sub>x</sub> nanocrystals into N/S Co-doped honeycomb-like 3D porous carbon for high-performance lithium storage. *Advanced Science* 5(9):1800829. <https://doi.org/10.1002/advs.201800829>
48. Tao L, Lin C-Y, Dou S, Feng S, Chen D, Liu D, Huo J, Xia Z, Wang S (2017) Creating coordinatively unsaturated metal sites in metal-organic-frameworks as efficient electrocatalysts for the oxygen evolution reaction: insights into the active centers. *Nano Energy* 41:417–425. <https://doi.org/10.1016/j.nanoen.2017.09.055>
49. Liu J, Shu T, Su L, Zhang X, Serpe MJ (2018) Synthesis of poly (N-isopropylacrylamide)-co-(acrylic acid) microgel-entrapped CdS quantum dots and their photocatalytic degradation of an organic dye. *RSC Adv* 8(30):16850–16857. <https://doi.org/10.1039/C8RA01855C>
50. Luo G, Shen K, Wu X, Zheng J, Xu C (2017) High contrast photoelectrochromic device with CdS quantum dot sensitized photoanode. *New J Chem* 41(2):579–587. <https://doi.org/10.1039/C6NJ02756C>
51. He Y, Wang Z, Ma L, Zhou L, Jiang Y, Gao J (2020) Synthesis of bismuth nanoparticle-loaded cobalt ferrite for electrochemical detection of heavy metal ions. *RSC Adv* 10(46):27697–27705. <https://doi.org/10.1039/D0RA02522D>
52. Beyene Y, Bitew Z, Fekade F (2022) Electrochemical detection of Pb (II) and Cd (II) using bismuth ferrite nanoparticle modified carbon paste electrodes. *Materials Advances* 3(14):5882–5892. <https://doi.org/10.1039/D2MA00133K>
53. Cesarino I, Cesarino V, Lanza MR (2013) Carbon nanotubes modified with antimony nanoparticles in a paraffin composite electrode: simultaneous determination of sulfamethoxazole and

- trimethoprim. *Sens Actuators, B Chem* 188:1293–1299. <https://doi.org/10.1016/j.snb.2013.08.047>
54. Silva MK, Cesarino I (2022) Electrochemical sensor based on Sb nanoparticles/reduced graphene oxide for heavy metal determination. *Int J Environ Anal Chem* 102(13):3109–3123. <https://doi.org/10.1080/03067319.2020.1763973>
55. Banerjee R, Phan A, Wang B, Knobler C, Furukawa H, O’Keeffe M, Yaghi OM (2008) High-throughput synthesis of zeolitic imidazolate frameworks and application to CO<sub>2</sub> capture. *Science* 319(5865):939–943. <https://doi.org/10.1126/science.1152516>
56. Du X-D, Wang C-C, Liu J-G, Zhao X-D, Zhong J, Li Y-X, Li J, Wang P (2017) Extensive and selective adsorption of ZIF-67 towards organic dyes: performance and mechanism. *J Colloid Interface Sci* 506:437–441. <https://doi.org/10.1016/j.jcis.2017.07.073>
57. Saracco G, Vankova S, Pagliano C, Bonelli B, Garrone E (2014) Outer Co (II) ions in Co-ZIF-67 reversibly adsorb oxygen from both gas phase and liquid water. *Phys Chem Chem Phys* 16(13):6139–6145. <https://doi.org/10.1039/C3CP54896A>
58. Li J, Wu Y-N, Li Z, Zhang B, Zhu M, Hu X, Zhang Y, Li F (2014) Zeolitic imidazolate framework-8 with high efficiency in trace arsenate adsorption and removal from water. *J Phys Chem C* 118(47):27382–27387. <https://doi.org/10.1021/jp508381m>
59. Bard AJ, Faulkner LR, Leddy J, Zoski CG (1980) *Electrochemical methods: fundamentals and applications*. Wiley, New York
60. Chen Y, Huang W, Chen K, Zhang T, Wang Y, Wang J (2019) Facile fabrication of electrochemical sensor based on novel core-shell PPy@ ZIF-8 structures: enhanced charge collection for quercetin in human plasma samples. *Sens Actuators, B Chem* 290:434–442. <https://doi.org/10.1016/j.snb.2019.04.006>
61. Sbei N, Martins GM, Shirinfar B, Ahmed N (2020) Electrochemical phosphorylation of organic molecules. *Chem Rec* 20(12):1530–1552. <https://doi.org/10.1002/tcr.202000096>
62. Sun S, Shan C, Yang Z, Wang S, Pan B (2021) Self-enhanced selective oxidation of phosphonate into phosphate by Cu(II)/H<sub>2</sub>O<sub>2</sub>: performance, mechanism, and validation. *Environ Sci Technol* 56(1):634–641. <https://doi.org/10.1021/acs.est.1c06471>
63. Sandford C, Edwards MA, Klunder KJ, Hickey DP, Li M, Barman K, Sigman MS, White HS, Minter SD (2019) A synthetic chemist’s guide to electroanalytical tools for studying reaction mechanisms. *Chem Sci* 10(26):6404–6422. <https://doi.org/10.1039/C9SC01545K>
64. Shanbhag YM, Shanbhag MM, Malode SJ, Dhanalakshmi S, Mondal K, Shetti NP (2022) 2D graphene sheets as a sensing material for the electroanalysis of zileuton. *Catalysts* 12(8):867. <https://doi.org/10.3390/catal12080867>
65. Huang K-J, Xu C-X, Xie W-Z, Wang WJC, Biointerfases SB (2009) Electrochemical behavior and voltammetric determination of tryptophan based on 4-aminobenzoic acid polymer film modified glassy carbon electrode. *Colloids Surf, B* 74(1):167–171. <https://doi.org/10.1016/j.colsurfb.2009.07.013>
66. Laviron E (1979) General expression of the linear potential sweep voltammogram in the case of diffusionless electrochemical systems. *J Electroanal Chem Interfacial Electrochem* 101(1):19–28. [https://doi.org/10.1016/S0022-0728\(79\)80075-3](https://doi.org/10.1016/S0022-0728(79)80075-3)
67. Bard AJ, Faulkner LR, White HS (2022) *Electrochemical methods: fundamentals and applications*. John Wiley & Sons
68. Gossner DK (1993) *Cyclic voltammetry: simulation and analysis of reaction mechanisms*, vol 43. VCH, New York
69. Bamford CH, Tipper C, Compton R (1986) *Electrode kinetics: principles and methodology*. Elsevier, New York, NY
70. Meits L (1965) *Polarographic techniques*, 2nd edn. Interscience Publishers, New York
71. El-Desoky H, Heinze J, Ghoneim M (2001) Electrodimerization of cyano-substituted derivatives of anthracene and naphthalene. *Electrochem Commun* 3(12):697–702. [https://doi.org/10.1016/S1388-2481\(01\)00241-7](https://doi.org/10.1016/S1388-2481(01)00241-7)
72. Samin A, Wu E, Zhang J (2017) The thermodynamic and transport properties of GdCl<sub>3</sub> in molten eutectic LiCl-KCl derived from the analysis of cyclic voltammetry signals. *J Appl Phys* 121(7). <https://doi.org/10.1063/1.4976570>
73. Kösemen A, Öztürk S, Şen Z, Kösemen ZA, Harbeck M, Öztürk ZZ (2017) Volatile organic compounds and dimethyl methyl phosphonate (DMMP) sensing properties of the metal oxide functionalized QCM transducers at room temperature. *J Electrochem Soc* 164(13):B657. <https://doi.org/10.1149/2.1251713jes>
74. Zhao Y, Du X, Wang X, He J, Yu Y, He H (2010) Effects of F doping on TiO<sub>2</sub> acidic sites and their application in QCM based gas sensors. *Sens Actuators, B Chem* 151(1):205–211. <https://doi.org/10.1016/j.snb.2010.09.020>
75. O’Neill M (2006) *The Merck index—an encyclopedia of chemicals, drugs, and biologicals*. Merck and Co., Inc., Whitehouse Station, NJ, USA, p 1204

**Publisher’s Note** Springer Nature remains neutral with regard to jurisdictional claims in published maps and institutional affiliations.